Detection of squeezed light with glass-integrated technology embedded into a homodyne detector setup

Carmen Porto,[1] Davide Rusca,[2,3] Simone Cialdi,[1,4] Andrea Crespi,[2,3] Roberto Osellame,[2,3] Dario Tamascelli,[1] Stefano Olivares,[1,4,*] and Matteo G. A. Paris[1,4]

[1]Quantum Technology Lab, Dipartimento di Fisica "Aldo Pontremoli," Università degli Studi di Milano, I-20133 Milan, Italy
[2]Istituto di Fotonica e Nanotecnologie–Consiglio Nazionale delle Ricerche, p.za Leonardo da Vinci 32, I-20133 Milan, Italy
[3]Dipartimento di Fisica, Politecnico di Milano, p.za Leonardo da Vinci 32, I-20133 Milan, Italy
[4]Istituto Nazionale di Fisica Nucleare, Sezione di Milano, Via Celoria 16, I-20133 Milan, Italy
*Corresponding author: stefano.olivares@fisica.unimi.it

We design and demonstrate a homodyne detection scheme based on a glass-integrated optical device (GID) operating in the quantum regime, that is, able to detect genuine nonclassical features. Our device is entirely fabricated by femtosecond laser micromachining. The GID incorporates on the same chip a balanced waveguide beamsplitter and a thermo-optic phase shifter, allowing us to record homodyne traces at different phases and to perform reliable quantum state tomography. In particular, we show that the GID allows for the detection of nonclassical features of continuous-variable quantum states, such as squeezed states. © 2018 Optical Society of America

1. INTRODUCTION

Balanced homodyne detection [1,2] is a powerful technique to detect and characterize nonclassical states of light, for example, to demonstrate squeezing [3–7] and to perform quantum tomography [8]. Homodyne detection is also a pivotal tool in continuous-variable quantum information processing [9,10], where information is encoded in the quadratures of the electromagnetic field. Indeed, several communication schemes and metrology protocols based on homodyne detection have been proposed and demonstrated [11–13]. More generally, the use of homodyne detection and continuous-variable quantum states is a promising avenue for quantum technologies, since they are robust against losses and may achieve deterministic and unconditional operation [14].

Scaling up the complexity in bulk optics encounters severe limitations, in particular concerning the optical phase stability and control, which is a crucial requirement for the manipulation of squeezed states. This makes the adoption of a monolithic integrated platform highly beneficial. Indeed, while integrated quantum photonics has recently boosted many experimental demonstrations and proposals based on discrete-variable systems [15–19], few on-chip experiments have been reported to date with continuous-variable systems. Fundamental operations for the manipulation of squeezed light

states within a reconfigurable silica-on-silicon chip have been demonstrated [20]. However, while thermal phase shifters were exploited to control the balance of the integrated beamsplitters (BSs), an external piezo-electric controller was used to vary the local-oscillator phase in the homodyne measurement. Very recently, the integration on the same chip of a BS and balanced detectors of the homodyne apparatus to perform tomography of coherent states and quantum random number generation has been reported [21], but no active modulation was operated on the phase of the local oscillator in the experiment. Moreover, glass waveguide directional couplers together with thermal phase shifters have been successfully used to implement single-photon quantum interference [22]. A few waveguide-based sources of squeezed light states have been also demonstrated [23,24], and first steps are moving toward a fully guided-wave based architecture exploiting squeezed light [25].

In this paper we report on a homodyne scheme that uses a glass-integrated-optics device, which is entirely fabricated by femtosecond laser micromachining. The device incorporates in the same chip both a balanced waveguide BS and a thermo-optic phase shifter (TOPS); we refer to it as glass-integrated optical device (GID). Photon detection is operated out of the chip.

As a matter of fact, by using the TOPS it is possible to acquire reliable homodyne traces by scanning different phases of

the local oscillator and, in turn, to detect nonclassical features of continuous-variable quantum states. In particular, we exploit GID to detect coherent and squeezed states and compare the results with those obtained via a standard homodyne detection (SHD) measurement, based on a balanced cube beamsplitter and a mechanical piezo movement.

The paper is structured as follows. In the next section we review the main features of standard homodyne detection and the main differences with our integrated homodyne analyzer. Section 3 is devoted to describing in detail our experimental apparatus, whereas Section 4 illustrates the use of GID to detect squeezing. Section 5 closes the paper with some concluding remarks.

2. STANDARD HOMODYNE DETECTION VERSUS INTEGRATED HOMODYNE ANALYZER

In a typical balanced homodyne measurement [26], the signal field has to be combined with a local oscillator (LO), namely a highly excited coherent state, by means of a 50:50 BS (top panel of Fig. 1). The two output beams are then detected by two photodiodes, and the difference photocurrent is recorded. It is well known, in fact, that a measurement of the difference of detected photocurrents is proportional to the generic quadrature of the electromagnetic field $\hat{X}(\theta) = \hat{a}e^{-i\theta} + \hat{a}^\dagger e^{i\theta}$, where θ is the relative phase between the LO and the signal described by the bosonic annihilation ($\hat{a}$) and creation ($\hat{a}^\dagger$) operators with $[\hat{a}, \hat{a}^\dagger] = \mathbb{I}$. Therefore, θ defines the phase of the quadrature under investigation and, upon varying it, one can perform the quantum-state tomography of the signal field [8]. In SHD, a cube BS is typically employed and θ is changed by a piezo-actuated mirror placed on the LO optical path, as sketched in the top panel of Fig. 1. In the case of the GID, this optical arrangement is replaced by a waveguide BS, which includes a TOPS; see the bottom panel of Fig. 1. Waveguides are directly inscribed in EAGLE XG (Corning) glass substrate by femtosecond laser writing technology [27,28]. To fabricate the waveguides, ultrashort pulses of about

300 fs duration, 240 nJ energy, and 1 MHz repetition rate, from a Yb:KYW cavity-dumped femtosecond laser oscillator, are focused 30 µm beneath the surface of the substrate through a 0.6 NA microscope objective. Nonlinear absorption processes of the ultrashort laser pulses generate a permanent refractive index increase, localized in the focal region. Translation of the sample under the laser beam at the constant speed of 20 mm/s allows one to directly inscribe the waveguide along the desired path; high precision translation is achieved by computer controlled air-bearing stages (Aerotech FiberGLIDE 3D). The waveguides support a single mode at 1064 nm wavelength (mode diameter $1/e^2$ is about 7 µm).

The directional coupler is composed of two waveguides, starting at the relative distance of 125 µm, and brought close at the distance of 11 µm for a length of 300 µm. In such a region, the waveguides exchange power by an evanescent field, and the interaction length is chosen to achieve a balanced splitting ratio. The bent segments have a curvature radius of 90 mm, which is the minimum that produces negligible additional bending losses.

To fabricate the dynamic phase shifter (the TOPS), a 55 nm gold layer is sputtered on top of the chip, and a resistor is patterned, by femtosecond laser pulses, above one of the input waveguides of the directional coupler. This technique is described in more detail in [29]. The resistor is 100 µm wide and 5 mm long, for a value of resistance of about 100 Ω. Thermal dissipation on the resistor, when driven with a suitable current, creates temperature gradients in the glass and thus thermo-optic modifications of the refractive indices in the waveguides. Therefore, a differential phase, directly proportional to the dissipated electrical power, can be imposed between the two input waveguides. In the homodyne measurements, the resistor is driven by a ramp generator (RG) to scan the LO phase at a frequency of 10 Hz, with a maximum voltage of 10 V. Average dissipated power is thus lower than 1 W.

In our experiments we aim at assessing the performance of the GID, also in comparison with the SHD. To this purpose, we employed an apparatus (see Section 3) where the two homodyne detection configurations involving the SHD and the GID, respectively, can be easily and quickly switched by means of flip mirrors. This apparatus in the SHD configuration has been already validated for the generation and detection of different kinds of squeezed states in past experiments [30,31].

The input signals are generated by using a subthreshold optical parametric oscillator (OPO), which allows us to generate squeezed light (see [30] for further details). The SHD configuration employs a cube BS, while the LO phase is scanned thanks to a piezo-mounted mirror, linearly driven by the RG. When, instead, the GID configuration is adopted, the signal from the OPO and the LO is coupled to the inputs of the GID by a single-mode fiber array; a multimode fiber array is then used to couple the outputs of the GID to the photodiodes (see Fig. 1). It is worth noting that a critical issue in our experiments is the minimization of the backreflections across the entire system. To avoid this situation, which induces instabilities in the OPO, the use of ferrule connector/angled physical contact connectors was found to be crucial. Light from the two
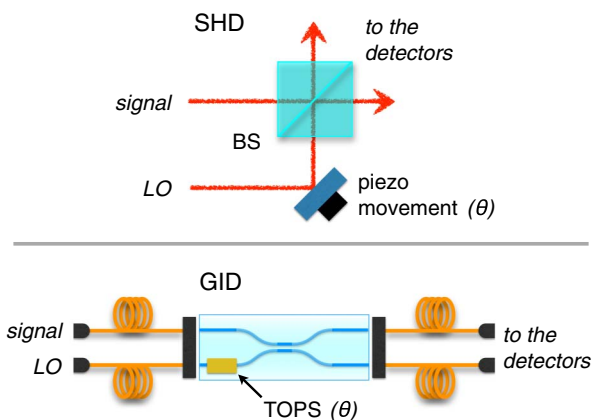

Fig. 1. (Top) SHD setup: signal and LO are mixed at a 50:50 BS, and the quadrature phase θ is scanned by means of a piezo movement. (Bottom) Integrated homodyne analyzer (GID): the BS is replaced by an integrated BS, and the phase θ is scanned by using a TOPS. Waveguides and fiber arrays are used to couple the input and output channels to the GID. See the text for details.

connectors is finally detected by two low-noise photodetectors, which are shared between the SHD and GID. The photocurrent difference is finally acquired and spectrally analyzed; further details are given in the next section and in [30].

3. EXPERIMENTAL SETUP

Figure 2 shows the whole scheme of our experimental apparatus. Continuous-wave squeezed light is generated by a sub-threshold OPO. The OPO input seed (1064 nm) and the OPO pump beam (532 nm) arise from a home-made internally frequency doubled Nd:YAG laser (Fig. 2). The laser source is based on a four-mirror ring cavity, and the active medium is a cylindrical Nd:YAG crystal (diameter 2 mm and length 60 mm) radially pumped by three arrays of water-cooled laser diodes at 808 nm. The crystal for the frequency doubling is a periodically poled MgO:LiNbO$_3$ (PPLN) of 10 mm, thermally stabilized around 70°C with a precision of 0.01°C. A light diode is placed inside the cavity in order to ensure the single mode operation. The output at 1064 nm is split into two beams by using a polarizing BS: one is used as the LO for the homodyne detector, and the other is sent into the OPO. The OPO cavity is linear with a free spectral range of 3300 MHz; the output mirror has a reflectivity of 91.7%, and the rear mirror 99.6%. A phase modulator generates a signal at frequency of 110 MHz (HF) used as active stabilization of the OPO cavity via the PoundDreverHall (PDH) technique [32]. In order to generate the coherent squeezed states our strategy is to exploit the combined effect of two optical modulators placed before the OPO [31]. The first modulator generates a coherent state with phase 0, while the second modulator generates a coherent state with phase $\pi/2$. By matching these coherent states with properly chosen amplitudes, it is possible

to generate coherent states for seeding the OPO on the sidebands with coherent amplitude up to $\approx$100 photons. Once the state is generated, the OPO output beam can be directed into either SHD or GID configurations by means of mirrors with high reflectivity at 1064 nm, mounted on flippers (see Fig. 2).

The SHD configuration employs a cube BS, while the LO phase is scanned thanks to a piezo-mounted mirror, linearly driven by the RG. When the mirrors are flipped up, the setup is switched to the GID configuration. In order to efficiently couple the signal from the OPO and the LO to the inputs of the GID we use a fiber array; a similar fiber array is used to couple the outputs of the GID to the photodiodes, as pictorially shown in Fig. 2. Each fiber array contains two fibers, fastened with high precision at a distance of 125 μm by means of quartz V-groove blocks. The input fibers, which yield single-mode and polarization-maintaining operation, are ferrule connector/physical contact connectorized. The signal and LO beams are coupled into them by means of adjustable FiberPort micropositioners. To improve the coupling efficiency, the built-in lenses of the latter components are chosen to ensure the optimal match between the incident modes and the fiber modes. The integrated-optics chip of the GID is placed on an aluminum holder to keep the substrate temperature uniform and stable. The two fiber arrays can be aligned accurately to the waveguide inputs and outputs by means of two six-axis positioning stages with micrometric resolution. Index-matching gel is used to eliminate reflection losses at the fiber–waveguide interfaces. The fibers in the output fiber array are instead multimode, with a core diameter of 50 μm and a cladding diameter of 125 μm, connectorized at the other ends with ferrule connector/angled physical contact (FC/APC) terminals to reduce backreflections.
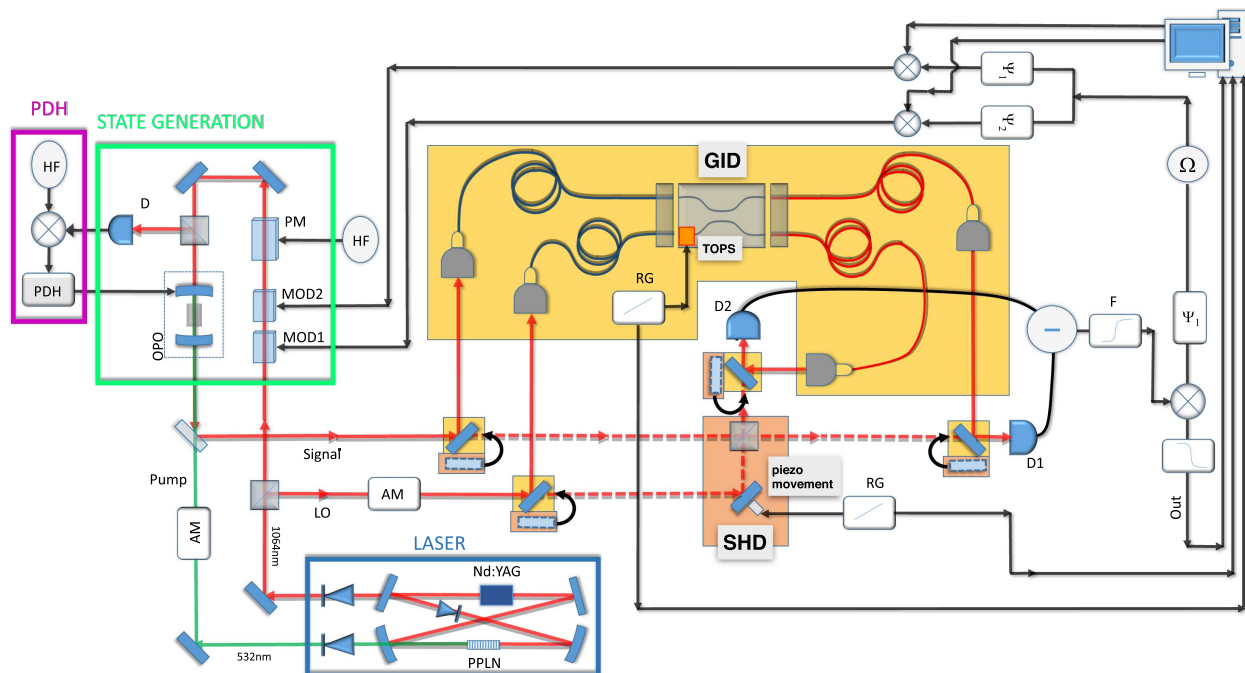

Fig. 2. Experimental setup for SHD and for the GID. In the latter case, a couple of fiber arrays are used for both entrance and exit facets of the GID to inject and eject signal and LO beams efficiently. The LO phase is changed thanks to a TOPS. See the text for further details.

Light from the two FC/APC connectors is finally collected by lenses and focused on low-noise photodetectors (D1, D2), which are shared between the two configurations SHD and GID. The information about the signal, at a frequency $\Omega = 3$ MHz, is retrieved by using an electronic apparatus which consists of a mixer ($\otimes$), a phase shifter set to ensure zero phase shift between the two inputs of the mixer, and a low-pass filter at 300 kHz; therefore the sensitivity to wavelength of the directional coupler is negligible due to the extremely small bandwidth of the squeezed light employed in the experiment. The two detectors are based on a free-space Fermionics photo-diode model FD500W and a LMH6624 operation amplifier in transimpedance configuration. The bandwidth is 7 MHz, and the electronic noise is 17 dB, below the vacuum noise at 3 MHz for 10 mW of the LO power.

The LO phase is spanned between 0 and 2π by using a RG. To perform the homodyne measurements, we collect $M = 7000$ data points in a time window of 800 ms with a repetition rate of 10 kHz. The sampling is triggered by a signal generated by the RG to ensure the synchronization between the acquisition process and the scanning of LO. The relative phase between the seed and the LO is not actively stabilized, and the phase fluctuation is $\approx 1°$ at ≈ 1 kHz (i.e., the mechanical resonance of the optical setup) and, thus, it can be safely neglected.

4. DETECTION OF SQUEEZING

As a first experiment, we characterize a squeezed vacuum state, generated by the OPO [30]. Figure 3 shows the experimental spectral homodyne traces achieved by collecting $M = 7000$ data points, $\{(x_k, \theta_k)\}$, x_k being the kth outcome from the measurement of the quadrature at LO phase θ_k, with $k = 1, \ldots, M$. They correspond to the vacuum squeezed states detected by switching between presets. In Fig. 3(a) we can see the homodyne trace acquired with the SHD, in which the LO phase is scanned from 0 to π. Figure 3(b), instead, shows the measurement performed employing the GID. All traces are normalized to the shot noise level of a pure vacuum field which is therefore set at one. In both cases the pump beam power for the OPO is $P = 300$ mW (well below the OPO threshold power $P_{\text{thr}} = 970$ mW, which is obtained by measurement of the classical parametric amplification for the OPO), and the LO power is set to 10 mW at the photodetectors, both for the GID and SHD configurations, by using an amplitude modulator. We emphasize that the level of the LO power is well within the linear working region of our photodiodes. For completeness we add that the power of the seed that we sent into the OPO both to stabilize the cavity and generate the signal in the sidebands at 3 MHz is only about few μW, and therefore negligible compared to the LO power.

As one can see from Fig. 3, the homodyne traces exhibit squeezing at $\theta = 0$ and antisqueezing at $\theta = \pi/2$. To perform the tomographic state reconstruction of the single-mode continuous-variable systems, we processed the experimental data through the pattern function method. This technique allows us to obtain the moments of given observables, such as quadratures, by averaging suitable kernel functions over the full set of the raw experimental data (see [8] for details). In our case, the experimental traces exhibit a Gaussian nature, witnessed by
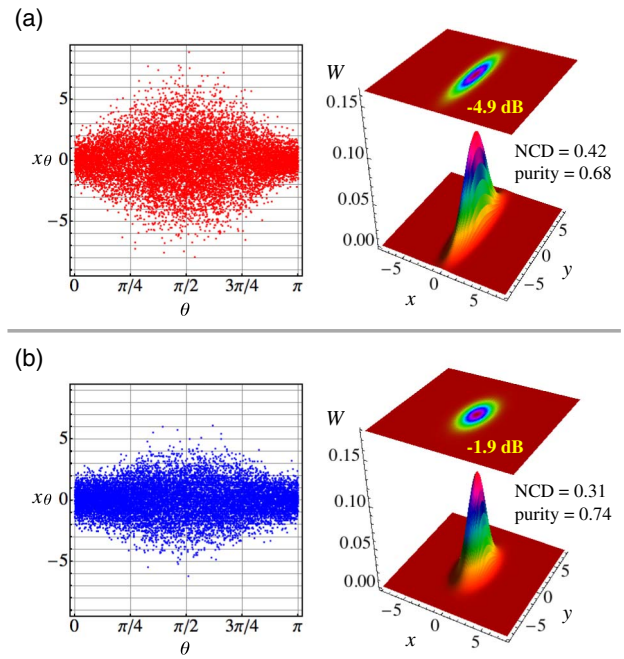

Fig. 3. Experimental homodyne traces referring to the vacuum squeezed states detected by using (a) the SHD and (b) the GID. We also report the corresponding reconstructed Wigner functions, the NCD, and the purity.

the kurtosis of the data sample. Therefore, the state is Gaussian and can be fully characterized by the first and second moments of the field quadratures at $\theta = 0$ and $\theta = \pi/2$ [10]. The reconstructed Gaussian Wigner functions, which correspond to the two examined cases, are displayed next to the respective homodyne traces in Fig. 3. The purity, $\mu[\rho] = \text{Tr}[\rho^2]$, and the nonclassical depth (NCD) [33] of the state ρ acquired with the SHD are $\mu = 0.68$ and NCD $= 0.42$ whereas those acquired with the GID are $\mu = 0.74$ and NCD $= 0.31$. It is worth noting that the higher purity of the state acquired by the GID is due to the presence of losses, which reduce the state energy and make it nearer to the vacuum state (which is pure). The chip is 20 mm long overall, giving an insertion loss of about 2.92 ± 0.08 dB at 1064 nm wavelength.

By using pattern function tomography, we can also evaluate the quadrature variance $\text{Var}[x_\theta]$ as a function of θ in order to highlight the difference between the squeezing and antisqueezing levels in the two measurement configurations. The results are shown in Fig. 4, where we plot tomographically reconstructed expectations of quadrature variance as functions of θ: the horizontal dashed line represents the vacuum noise level, and the observed noise levels for squeezing are -4.9 ± 0.5 dB for the SHD (blue) and -1.9 ± 0.1 dB for the GID (red), where the corresponding errors have been obtained by the tomographic analysis.

This difference arises from the different efficiencies of the two systems. Indeed, squeezed states that are observed in practical experiments necessarily suffer from losses in transmission channels and photodetectors that degrade the observed squeezing and antisqueezing levels. In order to analyze in more detail the effect of losses on the single-mode squeezed state,
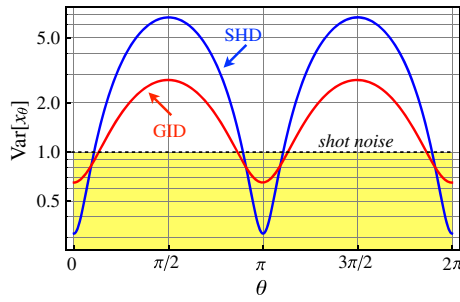
Fig. 4. Tomographically reconstructed quadrature variance as a function of θ for the SHD (blue) and the GID (red). We also report the shot-noise level for comparison (black horizontal dashed line). See the text for details.

we compare the performance of our apparatus with a theoretical model. The noise spectrum $\Delta^2 X_\pm$ of the squeezed (−) and antisqueezed (+) quadrature variances for an OPO below threshold can be written as [20,34,35]

$$\Delta^2 \hat{X}_\pm = 1 \pm \eta_{\text{tot}} \frac{4\sqrt{P/P_{\text{thr}}}}{\left(1 \mp \sqrt{P/P_{\text{thr}}}\right)^2 + 4\left(\frac{2\pi f}{\gamma}\right)^2}, \quad \textbf{(1)}$$

where $2\pi f/\gamma = 0.13$, f being the sideband frequency of the measurement and γ the OPO cavity decay rate. We also introduced the total system efficiency η_{tot}, which can be estimated by quantifying the individual contributions as $\eta_{\text{tot}} = \eta_{\text{DM}}\eta_{\text{esc}}\eta_{\text{HD}}\eta_{\text{D}}\eta_{\text{el}}$, where $\eta_{\text{DM}} = 0.96$ is the propagation efficiency of the optical path in the space between the OPO output coupler and the BS, the main amount of which comes from the measured dichroic mirror reflectivity; $\eta_{\text{D}} = 0.97$ is the quantum efficiency of photodiodes corresponding to the manufacturer specifications; $\eta_{\text{el}} = 0.98$ is the loss factor due to the electronic noise [36,37]; and $\eta_{\text{esc}} = 0.92$ is the OPO escape efficiency. Finally, η_{HD} is the homodyne detection efficiency, and its contribution is not the same in the two different configurations.

For the SHD setup, one simply has $\eta_{\text{HD}}^{(\text{SHD})} = \eta_{\text{Vis}}^{(\text{SHD})}$, where $\eta_{\text{Vis}}^{(\text{SHD})} \equiv \mathcal{V}^2$, $\mathcal{V}$ being the visibility, takes into account the degree of mode matching between OPO output mode and local oscillator LO in BS. The estimated visibility $\mathcal{V}$ in the case of SHD is 0.96, and it is achieved by direct measurement of the interference signal between the two beams at the BS.

When, instead, the GID is used, we should take into account the overall GID efficiency, η_{GID}. Therefore, we have $\eta_{\text{HD}}^{(\text{GID})} = \eta_{\text{Vis}}^{(\text{GID})}\eta_{\text{GID}}$, with $\eta_{\text{Vis}}^{(\text{GID})} = 0.96$ (the estimated visibility is $\mathcal{V} = 0.98$) and $\eta_{\text{GID}} = \eta_{\text{f}}\eta_{\text{w}}$, where η_{f} and η_{w} are the fiber coupling and the waveguide transmission efficiencies, respectively. The high visibility certifies that the polarization at the GID output is preserved as well as the spatial mode matching. The actual value η_{GID} has been evaluated by measuring the input intensity into the fiber coupling lens and the output intensity at the multimode fiber exit. Since the measured fibers coupling efficiency is $\eta_{\text{f}} = 0.82$, we estimate $\eta_{\text{w}} = 0.51$. We use an optical gel between the waveguide and the fiber in order to avoid the reflections; thus the value of η_{w} is due to waveguide propagation losses and fiber-to-waveguide mode mismatch and
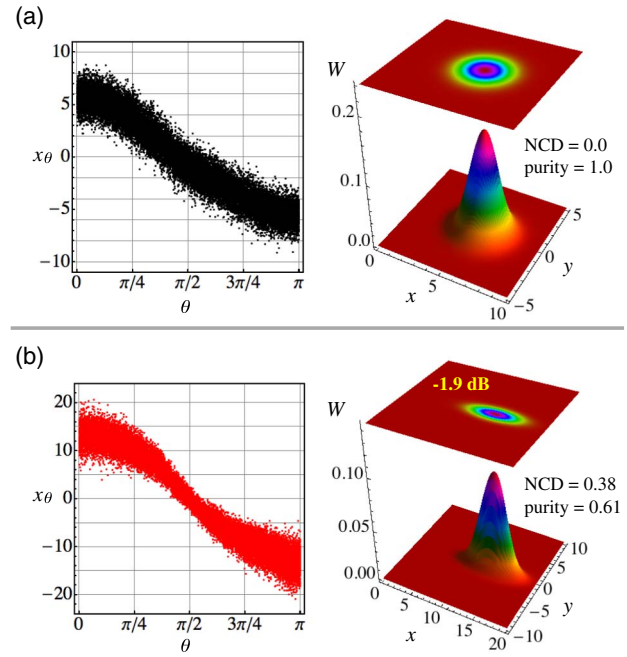

Fig. 5. (a) Experimental homodyne trace referring to a CS by exploiting the GID and the corresponding reconstructed Wigner function. (b) Experimental homodyne trace and reconstructed Wigner functions of squeezed CS by using the GID. Their NCDs and purities are also reported.

misalignment. It is worth noting that the chip does not alter the features of the generated states but acts as a lossy channel. Thus, its effect is merely to degrade the observed squeezing level.

Our experimental setup has the capability to generate different kinds of squeezed states on demand by injecting states with controlled amplitude and/or phase distributions into the OPO [31]. In the presence of a coherent state (CS) we obtain the homodyne trace reported in Fig. 5(a). More in detail, in order to obtain a CS with desired amplitude and phase, we exploit the two modulators placed before the OPO, and at the same time we block the pump. In the case shown in Fig. 5(a), the two modulators shift a very low power on the sidebands at 3 MHz in order to obtain a CS with about six photons. Considering that we use a low pass filter of 300 kHz to retrieve the signal, in this case the power level on the two sidebands is about 300 fW. We can see that the GID allows us to record the signal at different phases scanned by the thermo-optic phase shifter. Moreover, the tomographically reconstructed Wigner function corresponds to a CS with purity 1 and vanishing NCD, as expected.

When we add the pump, we observe the phase squeezed CS shown in Fig. 5(b): the observed level for squeezing at $\theta = \pi/2$ is -1.9 ± 0.2 dB. In this case the pump and the signal on the sidebands have the same phase.

5. CONCLUSIONS

In this work we have studied a homodyne detection scheme exploiting a glass-integrated-optics device entirely fabricated by femtosecond laser micromachining, the GID. We have

compared the performance of the GID-based scheme with the standard counterpart based on a bulk BS and mechanical phase shifter. In particular, the recorded experimental homodyne traces are reliable enough to perform the tomographic reconstruction of typical continuous-variable optical states, such as CSs and nonclassical squeezed CSs. Therefore, we have demonstrated that, despite large losses, our integrated device allows us to detect the nonclassical features of the input signals. Overall, our results show that GID is highly reliable also with respect to the standard homodyne technique based on a cube BS and a piezo-mounted movement to scan the field quadratures.

Future work will aim at reducing the device losses by further optimization of the waveguide writing process, in particular by performing post-inscription thermal annealing [38]. This will enable a substantial increase of the overall device efficiency and will also allow for more compact device size with reduced waveguide bending radii. The operating frequency of the phase shifter is limited by the heat diffusion dynamics in the substrate; future optimizations of the circuit geometry and distance from the heaters may allow reaching modulation speeds in the hundreds of Hz range, as is achieved in standard silica-on-silicon lithographic technology [39]. The GID may however already be operated in the quantum regime and embedded in quantum optics setups for the quantum characterization of continuous-variable states. Fiber coupled detectors may be connected with high efficiency to this kind of device. In addition, our device may be exploited in hybrid detection schemes, which join photon number resolving detectors to homodyne-like techniques [40,41], to implement continuous-variable quantum key distribution protocols based on coherent states [42–44].

Analogous GID operating at telecom wavelength range can be realized with no additional difficulties [29], thus opening interesting perspectives for integration within optical fiber networks. Our results pave the way to the applications of the GID in quantum information protocols involving continuous-variable optical systems which require integrated configurations, such as the simulation of non-Markovian evolution via linear optics [45].

REFERENCES

1. H. P. Yuen and V. W. S. Chan, "Noise in homodyne and heterodyne detection," Opt. Lett. **8**, 177–179 (1983).
2. G. L. Abbas, V. W. S. Chan, and T. K. Yee, "Local-oscillator excess-noise suppression for homodyne and heterodyne detection," Opt. Lett. **8**, 419–421 (1983).
3. E. Jakeman, C. J. Oliver, and E. R. Pike, "Optical homodyne detection," Adv. Phys. **24**, 349–405 (1975).
4. B. L. Schumaker, "Noise in homodyne detection," Opt. Lett. **9**, 189–191 (1984).
5. G. M. D'Ariano, C. Macchiavello, and M. G. A. Paris, "Detection of the density matrix through optical homodyne tomography without filtered back projection," Phys. Rev. A **50**, 4298–4302 (1994).
6. G. Breitenbach, S. Schiller, and J. Mlynek, "Measurement of the quantum states of squeezed light," Nature **387**, 471–475 (1997).
7. A. I. Lvovsky and M. G. Raymer, "Continuous-variable optical quantum-state tomography," Rev. Mod. Phys. **81**, 299–332 (2009).
8. G. M. D'Ariano, M. G. A. Paris, and M. F. Sacchi, "Quantum tomography," Adv. Imag. Electr. Phys. **128**, 205–308 (2003).
9. C. Weedbrook, S. Pirandola, R. García-Patrón, N. J. Cerf, T. C. Ralph, J. H. Shapiro, and S. Lloyd, "Gaussian quantum information," Rev. Mod. Phys. **84**, 621–669 (2012).
10. S. Olivares, "Quantum optics in the phase space," Eur. Phys. J. Spec. Top. **203**, 3–24 (2012).
11. S. Olivares, S. Cialdi, F. Castelli, and M. G. A. Paris, "Homodyne detection as a near-optimum receiver for phase-shift keyed binary communication in the presence of phase diffusion," Phys. Rev. A **87**, 050303(R) (2013).
12. P. Jouguet, S. Kunz-Jacques, A. Leverrier, P. Grangier, and E. Diamanti, "Experimental demonstration of long-distance continuous-variable quantum key distribution," Nat. Photonics **7**, 378–381 (2013).
13. A. A. Berni, T. Gehring, B. M. Nielsen, V. Händchen, M. G. A. Paris, and U. L. Andersen, "Ab initio quantum-enhanced optical phase estimation using real-time feedback control," Nat. Photonics **9**, 577–581 (2015).
14. J. L. O'Brien, A. Furusawa, and J. Vuckovic, "Photonic quantum technologies," Nat. Photonics **3**, 687–695 (2009).
15. A. Politi, M. J. Cryan, J. G. Rarity, S. Yu, and J. L. O'Brien, "Silica-on-silicon waveguide quantum circuits," Science **320**, 646–649 (2008).
16. L. Sansoni, F. Sciarrino, G. Vallone, P. Mataloni, A. Crespi, R. Ramponi, and R. Osellame, "Polarization entangled state measurement on a chip," Phys. Rev. Lett. **105**, 200503 (2010).
17. J. M. Silverstone, D. Bonneau, J. L. O'Brien, and M. Thompson, "Silicon quantum photonics," IEEE J. Sel. Top. Quantum Electron. **22**, 390–402 (2016).
18. T. Meany, M. Gräfe, R. Heilmann, A. Perez-Leija, S. Gross, M. J. Steel, M. J. Withford, and A. Szameit, "Laser written circuits for quantum photonics," Laser Photon. Rev. **9**, 363–384 (2015).
19. D. Tamascelli, S. Olivares, S. Rossotti, R. Osellame, and M. G. A. Paris, "Quantum state transfer via Bloch oscillations," Sci. Rep. **6**, 26054 (2016).
20. G. Masada, K. Miyata, A. Politi, T. Hashimoto, J. L. O'Brien, and A. Furusawa, "Continuous-variable entanglement on a chip," Nat. Photonics **9**, 316–319 (2015).
21. F. Raffaelli, G. Ferranti, D. H. Mahler, P. Sibson, J. E. Kennard, A. Santamato, G. Sinclair, D. Bonneau, M. G. Thompson, and J. C. F. Matthews, "A homodyne detector integrated onto a photonic chip for measuring quantum states and generating random numbers," Quantum Sci. Technol. **3**, 025003 (2018).
22. B. J. Smith, D. Kundys, N. Thomas-Peter, P. G. R. Smith, and I. A. Walmsley, "Phase-controlled integrated photonic quantum circuits," Opt. Express **17**, 13516–13525 (2009).
23. A. Dutt, K. Luke, S. Manipatruni, A. L. Gaeta, P. Nussenzveig, and M. Lipson, "On-chip optical squeezing," Phys. Rev. Appl. **3**, 044005 (2015).
24. M. Stefszky, R. Ricken, C. Eigner, V. Quiring, H. Herrmann, and C. Silberhorn, "Waveguide cavity resonator as a source of optical squeezing," Phys. Rev. Lett. **7**, 044026 (2017).
25. F. Kaiser, B. Fedrici, A. Zavatta, V. D'Auria, and S. Tanzilli, "A fully guided-wave squeezing experiment for fiber quantum networks," Optica **3**, 362–365 (2016).
26. H.-A. Bachor and T. C. Ralph, *A Guide to Experiments in Quantum Optics* (Wiley-VCH, 2004).
27. S. M. Eaton, H. Zhang, M. L. Ng, J. Li, W. Chen, S. Ho, and P. R. Herman, "Transition from thermal diffusion to heat accumulation in high repetition rate femtosecond laser writing of buried optical waveguides," Opt. Express **16**, 9443–9458 (2008).

28. R. Osellame, G. Cerullo, and R. Ramponi, *Topics in Applied Physics, Femtosecond Laser Micromachining: Photonic and Microfluidic Devices in Transparent Materials* (Springer, 2012).
29. F. Flamini, L. Magrini, A. S. Rab, N. Spagnolo, V. D'Ambrosio, P. Mataloni, F. Sciarrino, T. Zandrini, A. Crespi, R. Ramponi, and R. Osellame, "Thermally reconfigurable quantum photonic circuits at telecom wavelength by femtosecond laser micromachining," Light Sci. Appl. **4**, e354 (2015).
30. S. Cialdi, C. Porto, D. Cipriani, S. Olivares, and M. G. A. Paris, "Full quantum state reconstruction of symmetric two-mode squeezed thermal states via spectral homodyne detection and a state-balancing detector," Phys. Rev. A **93**, 043805 (2016).
31. A. Mandarino, M. Bina, C. Porto, S. Cialdi, S. Olivares, and M. G. A. Paris, "Assessing the significance of fidelity as a figure of merit in quantum state reconstruction of discrete and continuous-variable systems," Phys. Rev. A **93**, 062118 (2016).
32. R. W. P. Drever, J. L. Hall, F. V. Kowalski, J. Hough, G. M. Ford, A. J. Munley, and H. Ward, "Laser phase and frequency stabilization using an optical resonator," Appl. Phys. B **31**, 97–105 (1983).
33. C. T. Lee, "Measure of the nonclassicality of nonclassical states," Phys. Rev. A **44**, R2775–R2778 (1991).
34. H. Vahlbruch, M. Mehmet, K. Danzmann, and R. Schnabel, "Detection of 15 dB squeezed states of light and their application for the absolute calibration of photoelectric quantum efficiency," Phys. Rev. Lett. **117**, 110801 (2016).
35. T. Aoki, G. Takahashi, and A. Furusawa, "Squeezing at 946 nm with periodically poled KtiOPO$_4$," Opt. Express **14**, 6930–6935 (2006).
36. J. Appel, D. Hoffman, E. Figueroa, and A. I. Lvovsky, "Electronic noise in optical homodyne tomography," Phys. Rev. A **75**, 035802 (2007).
37. M. Esposito, F. Benatti, R. Floreanini, S. Olivares, F. Randi, K. Titimbo, M. Pividori, F. Novelli, F. Cilento, F. Parmigiani, and D. Fausti, "Pulsed homodyne Gaussian quantum tomography with low detection efficiency," New. J. Phys. **16**, 043004 (2014).
38. A. Arriola, S. Gross, N. Jovanovic, N. Charles, P. G. Tuthill, S. M. Olaizola, A. Fuerbach, and M. J. Withford, "Low bend loss waveguides enable compact, efficient 3D photonic chips," Opt. Express **21**, 2978–2986 (2013).
39. N. Takato, K. Jinguji, M. Yasu, H. Toba, and M. Kawachi, "Silica-based single-mode waveguides on silicon and their application to guided-wave optical interferometers," J. Lightwave Technol. **6**, 1003–1010 (1988).
40. M. Bina, A. Allevi, M. Bondani, and S. Olivares, "Homodyne-like detection for coherent state-discrimination in the presence of phase noise," Opt. Express **25**, 10685–10692 (2017).
41. M. Bina, A. Allevi, M. Bondani, and S. Olivares, "Phase-reference monitoring in coherent-state discrimination assisted by a photon-number resolving detector," Sci. Rep. **6**, 26025 (2016).
42. F. Grosshans and P. Grangier, "Continuous variable quantum cryptography using coherent states," Phys. Rev. Lett. **88**, 057902 (2002).
43. F. Grosshans, G. Van Assche, J. Wenger, R. Brouri, N. J. Cerf, and P. Grangier, "Quantum key distribution using Gaussian-modulated coherent states," Nature **421**, 238–241 (2003).
44. M. Cattaneo, M. G. A. Paris, and S. Olivares, "Hybrid quantum key distribution using coherent states and photon-number-resolving detectors," arXiv:1707.02852 [quant-ph].
45. J. Jin, V. Giovannetti, R. Fazio, F. Sciarrino, P. Mataloni, A. Crespi, and R. Osellame, "All-optical non-Markovian stroboscopic quantum simulator," Phys. Rev. A **91**, 012122 (2015).